Excitation of high-latitude MAC waves in Earth's core

Quentin Nicolas [ORCID] and Bruce Buffett

Department of Earth and Planetary Sciences, University of California, Berkeley, CA 94720, USA E-mail: qnicolas@berkeley.edu

SUMMARY

Recent geomagnetic observations reveal localized oscillations in the field's secular acceleration at high latitudes, with periods of about 20 yr. Several types of waves in rotating magnetized fluids have been proposed to explain equatorial oscillations with similar high frequencies. Among these are non-axisymmetric Alfvén waves, magneto-Coriolis waves and, in the presence of fluid stratification, magnetic-Archimedes–Coriolis (MAC) waves. We explore the hypothesis that the observed high latitude patterns are the signature of MAC waves by modelling their generation in Earth's core. We quantitatively assess several generation mechanisms using output from dynamo simulations in a theoretical framework due to Lighthill. While the spatio-temporal structure of the sources from the dynamo simulations are expected to be realistic, their amplitudes are extrapolated to reflect differences between the simulation's parameter space and Earth-like conditions. We estimate full wave spectra spanning monthly to centennial frequencies for three plausible excitation sources: thermal fluctuations, Lorentz force and magnetic induction. When focusing on decadal frequencies, the Lorentz force appears to be most effective in generating high-latitude MAC waves with amplitude estimates falling within an order of magnitude of observed oscillations. Overall, this study puts forward MAC waves as a viable explanation, in the presence of fluid stratification at the top of Earth's core, for observed field variations at high latitudes.

**Key words:** Rapid time variations; Satellite magnetics; Core dynamics.

1 INTRODUCTION

Satellite-based observations at a high temporal sampling (Olsen *et al.* 2000; Friis-Christensen *et al.* 2006; Maus 2007) reveal localized fluctuations on short timescales compared with the century-long convective overturn times. The spatial pattern of the fluctuations are reminiscent of known wave motion for several types of waves in rotating magnetic fluids. Understanding potential generation processes for these waves offers an indirect, yet insightful way of probing the convective processes that generate these waves.

A steady core surface flow accounts for most of the geomagnetic field variations (Bloxham 1992), obscuring the fingerprint of short-period waves in the first time derivative of the field. Those features are best detected in the second time derivative of the field, also called secular acceleration (SA). Space-based field measurements from the last two decades have enabled estimates of SA up to spherical harmonic degree 16 (CHAOS models, see e.g Finlay *et al.* 2020). A snapshot of the northern hemispheric radial SA at the core surface in 2016.0, estimated with CHAOS-7.12, is shown in Fig. 1. Four patches of alternating signs, corresponding to spatial oscillations of angular order 3, are visible from Northern Canada to Siberia, with strongest amplitude under Eastern Siberia. Chi-Durán *et al.* (2020) found that the dominant mode of variability in this signal is a westward-travelling pattern of amplitude 1.5 μT

yr^{-2} and period 21 yr. Higher order waves with similar periods, both eastward and westward travelling, are also reported in the equatorial region.

Dynamical theory and numerical modelling demonstrate various types of waves that can propagate within the outer core at decadal periods (e.g. Gillet *et al.* 2022). The presence of rapid rotation and magnetic effects gives rise to three main categories defined by the two forces that dominate their balance: Inertial waves (inertia and Coriolis effects), Alfvén waves (inertia and Lorentz force) and magneto-Coriolis (MC) waves (Coriolis and Lorentz forces). While some slow inertial modes in a spherical shell can attain decadal periods (Zhang *et al.* 2001), their propagation direction is not compatible with the high-latitude signal of interest in this study. Axisymmetric Alfvén waves (also called torsional waves) have been detected in core flow models with a period of around 6 yr (Gillet *et al.* 2010). Their zonally invariant nature, however, argues against them as a candidate for the waves portrayed in Fig. 1. Aubert & Finlay (2019) found non-axisymmetric Alfvén waves in a very high-resolution simulation of core dynamics. These waves have a columnar structure characteristic of quasi-geostrophy (QG) and propagate outward from rising plumes, focusing their power at the equator; this renders them incompatible with high-latitude oscillations. Planetary-scale MC waves have periods that are too long, although Hori *et al.* (2015) and Gerick *et al.* (2021) recently showed that smaller scale waves for
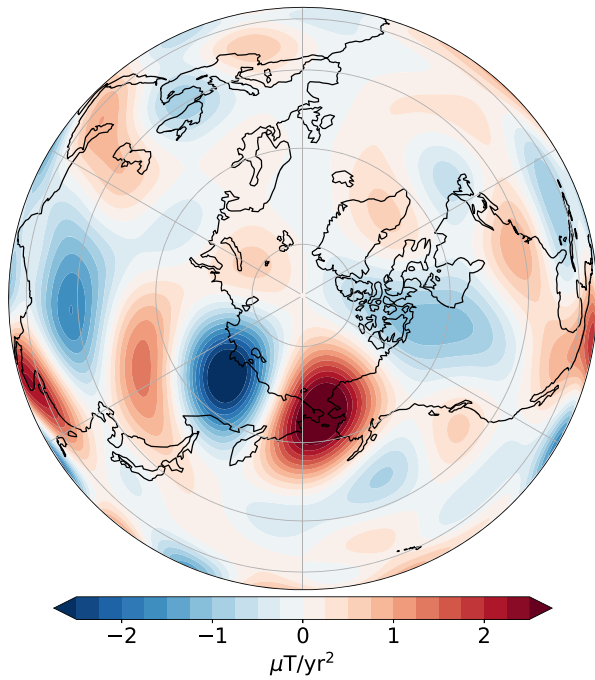
Figure 1. Snapshot of the core-surface geomagnetic acceleration from the CHAOS-7.12 model over the Northern Hemisphere, in 2016.0 (truncated at spherical harmonic degree $l = 13$).

a realistic magnetic field configuration could have frequencies compatible with observed waves. However, their high damping rates are potentially incompatible with the observed longevity of the Northern Hemisphere SA pattern, which has been travelling with modest damping for 20 yr (Chi-Durán *et al.* 2021).

Another mechanism leading to higher frequency oscillations is due to the presence of stable stratification, adding a third restoring force to create so-called magnetic–Archimedes–Coriolis (MAC) waves (Braginsky 1993). Whether or not such a stably stratified region exists at the top of the core is subject to debate both within the seismological and geomagnetic communities (see e.g. van Tent *et al.* 2020; Gastine *et al.* 2020). This work takes its existence as a premise, and shows that such a layer can support high-latitude waves compatible with observations. MAC waves have already been proposed to explain axisymmetric oscillations (Buffett 2014; Buffett & Knezek 2018) and equatorial waves (Buffett & Matsui 2019). Previous models for non-zonal MAC waves included analytical treatments on a β-plane (i.e. neglecting sphericity; Braginsky 1998) and more complex numerical models in spherical shells with arbitrary field and stratification configurations (e.g. Knezek & Buffett 2018). Buffett & Matsui (2019) recently derived a fully spherical analytical model, which is shown here to represent equatorial and high-latitude oscillations in a unified framework.

The presence of waves requires the existence of a generation mechanism. Modelling this excitation offers a way to put quantitative constraints on convective processes inside the core. By matching observed and modelled wave amplitudes, we can draw inferences about the strength of the convective forcings. Geodynamo models are capable of reaching the so-called MAC balance, which is thought to be relevant for conditions in the core (Aubert *et al.* 2017). If the model conditions are close enough to actual Earth values, one could infer the wave generation directly from a simulation. One example is the recent study of Aubert & Finlay (2019), which

identified buoyancy fluctuations as the main source of QG Alfvén waves. A lower-resolution model may overly damp the waves of interest, making direct simulations less feasible. Still, if the simulations reproduce a MAC balance, one can use such a model to constrain the spatial and temporal pattern of sources. The amplitude of the sources can then be extrapolated to Earth-like conditions (see Buffett & Knezek 2018), making it possible to link the observed wave amplitudes with viable source mechanisms.

This work expands upon earlier theory for MAC waves in a spherical shell (Buffett & Matsui 2019) to take into account wave excitation. A general framework to solve for forced MAC waves with arbitrary spatio-temporal forcing patterns is presented, and used with source terms evaluated from a suitable geodynamo model. It is shown that observed patterns and non-axisymmetric high-latitude MAC waves have similar features, and that when extrapolated to core conditions, magnetic stresses are the strongest excitation source and predict realistic wave amplitudes. This advances MAC waves as a potential candidate for the observed high-latitude SA oscillations.

2 DESCRIPTION AND NUMERICAL TREATMENT OF MAC WAVES

This section presents the analytical and numerical treatment of forced MAC waves in a thin, rotating, stratified shell filled with an electrically conducting fluid. The basic premises are identical to Buffett & Matsui (2019), hence we only give a brief overview of the assumptions required to build the analytical model. Upon discretization, waves appear as eigenvectors of a linear matrix operator. We show how forced waves can be decomposed on the non-orthogonal basis formed by these eigenvectors.

2.1 Analytical model for forced MAC waves

Waves are modelled as small perturbations on a background state at rest, with a known spatially varying magnetic field $\boldsymbol{B}_0(\boldsymbol{x})$ and a fixed density stratification ρ_0. None of these background fields change with time t. The perturbations in velocity, magnetic field and density are denoted by $\boldsymbol{v}(\boldsymbol{x}, t)$, $\boldsymbol{b}(\boldsymbol{x}, t)$ and $\rho_1(\boldsymbol{x}, t)$, respectively. Because the shell thickness H is an order of magnitude smaller than the horizontal length scale of the waves of interest ($L \simeq 2000$ km), continuity requires the radial component of the velocity to be small compared with its horizontal components. Several approximations stem from these conditions:

(i) The vertical force balance is hydrostatic to the leading order.

(ii) The density perturbations due to radial wave motion are small, which justifies the use of the Boussinesq approximation with a constant reference density ρ_0 in the inertial terms.

(iii) Only the radial component of rotation is retained in the Coriolis term due to the smallness of radial motions.

(iv) The condition $H \ll L$ means that radial gradients in $\boldsymbol{b}$ and $\boldsymbol{v}$ are large compared with horizontal gradients. Assuming that all components of $\boldsymbol{B}_0$ have the same order of magnitude, this yields $\boldsymbol{B}_0 \cdot \nabla \simeq B_{0r}\partial_r$, where B_{0r} is the radial component of the background magnetic field.

(v) Gradients in large-scale quantities are supposed to be much smaller than the (radial) gradients in wave quantities.

The last two approximations simplify the treatment of the magnetic tension and induction terms. The linearized Lorentz force becomes $\mu^{-1}\boldsymbol{B}_0 \cdot \nabla \boldsymbol{b} \simeq B_{0r}\partial_r \boldsymbol{b}$, where μ is the permeability of free space. Similarly the linearized induction term becomes

$\nabla \times (\boldsymbol{v} \times \boldsymbol{B}_0) \simeq B_{0r} \partial_r \boldsymbol{v}$. In spherical coordinates (r, θ, λ—radial distance, colatitude, longitude), the momentum, induction, continuity and mass conservation equations become

$$\partial_r p = -\rho_1 g + \rho_0 F_r \tag{1}$$

$$\partial_t v_\theta - 2\Omega \cos\theta \ v_\lambda = -\frac{1}{\rho_0 R} \partial_\theta p + \frac{1}{\rho_0 \mu} B_{0r} \partial_r b_\theta + F_\theta \tag{2}$$

$$\partial_t v_\lambda + 2\Omega \cos\theta \ v_\theta = -\frac{1}{\rho_0 R \sin\theta} \partial_\lambda p + \frac{1}{\rho_0 \mu} B_{0r} \partial_r b_\lambda + F_\lambda \tag{3}$$

$$(\partial_t - \eta \nabla^2)\boldsymbol{b} = B_{0r} \partial_r \boldsymbol{v} + \boldsymbol{F}_I \tag{4}$$

$$\nabla \cdot \boldsymbol{v} = \nabla \cdot \boldsymbol{b} = 0 \tag{5}$$

$$\partial_t \rho_1 = -v_r \partial_r \rho_0, \tag{6}$$

where p and ρ_1 denote the pressure and density perturbations carried by the waves and g is the acceleration of gravity at R, the core–mantle boundary (CMB) radius. Other terms appearing here are Earth's rotation rate Ω, and the fluid's magnetic diffusivity η. We have included a generic forcing term $\boldsymbol{F}$ in the momentum equations, $\boldsymbol{F}_I$ in the induction equations. The specific form of these forcing terms is based on the approach of Lighthill (1952).

Boundary conditions for those waves are detailed in Buffett & Matsui (2019), and consist of no-penetration at the CMB, zero horizontal velocities at the base of the layer and zero horizontal magnetic perturbations at the top and bottom of the layer. Rigorously speaking, the latter condition should be applied below a skin depth over which magnetic perturbations penetrate the interior. This skin depth (given by $\delta = \sqrt{2\eta/\omega}$ with ω the wave frequency, $\delta \simeq 10$ km for a 20-yr wave) is small in comparison with the assumed layer depth (140 km, see Section 2.3). Numerical calculations of the waves with and without an explicit treatment of the skin depth justifies our choice of the magnetic boundary condition at the base of the layer.

2.2 MAC wave forcing by convection

We are now in possession of a model for unforced waves, and turn to the description of the wave generation. We propose that these waves are excited by large-scale convective motions below the stratified layer. Wave generation by internal processes is described by an approach first introduced by Lighthill (1952). One of the underlying assumptions is that wave processes do not greatly influence the convective (waveless) fluid motions. However, there is no attempt to separate the motion into convective and wave-like parts. Instead the equations governing the full fluid motion inside the wave region are written as the sum of a wave equation and a correction term. This correction includes terms that must be added to the wave equations to obtain an exact description the full governing equations. We illustrate the approach with the induction equation before offering a physical interpretation. The exact form of the induction equation is

$$\partial_t \boldsymbol{B} + \boldsymbol{V} \cdot \nabla \boldsymbol{B} = \boldsymbol{B} \cdot \nabla \boldsymbol{V} + \eta \nabla^2 \boldsymbol{B}. \tag{7}$$

We write it as the sum of a wave equation acting on $\boldsymbol{V}$ and $\boldsymbol{B}$ and a correction term:

$$(\partial_t - \eta \nabla^2)\boldsymbol{B} - B_{0r} \partial_r \boldsymbol{V} = -\boldsymbol{V} \cdot \nabla \boldsymbol{B} + \boldsymbol{B} \cdot \nabla \boldsymbol{V} - B_{0r} \partial_r \boldsymbol{V}. \tag{8}$$

The terms on the right-hand-side of eq. (8) are associated the forcing term $\boldsymbol{F}_I$ in eq. (4). Specific the forcing term $\boldsymbol{F}_I$ becomes

$$\boldsymbol{F}_I = \nabla \times (\boldsymbol{V} \times \boldsymbol{B}) - B_{0r} \partial_r \boldsymbol{V}. \tag{9}$$

In the Lighthill approach we assume that $\boldsymbol{F}_I$ can be evaluated using the convective parts of $\boldsymbol{V}$ and $\boldsymbol{B}$ because the wave motion is assumed to be small. Recall that this was the justification in Section 2.1 to linearize the governing equations for the wave motion. The Lighthill approach also assumes that the left-hand side of eq. (8) represents the wave motion. There are several ways to think about this. We might appeal to a separation of timescales between the waves and the convective flow to justify letting most of the time variation in $\boldsymbol{B}$ be due to wave motion. Alternatively, we might appeal to spatial separation because convection is mostly confined to the region below the stratified layer and the wave motion is confined to the stratified layer. Conceptually, the convective motion is producing variations in density, magnetic and electric fields, which collectively serve as 'seeds' for wave motion. We assume there is no feedback of this wave motion on the convection.

The Lighthill approach has been successfully applied to the problem of sound generation by turbulent flow (Lighthill 1952). It has also been tested in the problem of internal wave generation in a layer above a vigorously convecting fluid (Lecoanet *et al.* 2015). We extend the approach here to the problem of MAC wave generation due to convection in an underlying region.

Applying the Lighthill approach to the Boussinesq momentum equation yields additional forcing terms. The full momentum equation is

$$\partial_t \boldsymbol{V} + \boldsymbol{V} \cdot \nabla \boldsymbol{V} + 2\Omega \cos(\theta) \hat{\boldsymbol{z}} \times \boldsymbol{V} = -\frac{1}{\rho_0} \nabla P$$
$$-\frac{\tilde{\rho}}{\rho_0} \boldsymbol{g} + \frac{1}{\rho_0 \mu} \boldsymbol{B} \cdot \nabla \boldsymbol{B}, \tag{10}$$

where $\tilde{\rho}$ is the difference between the full density and the background state ρ_0. This means that the pressure P represents the dynamic pressure fluctuation relative to the hydrostatic pressure based on ρ_0. It also means that $\tilde{\rho}$ contains both the convective density fluctuations and the fluctuations due to wave motion. Recall that the wavelike density perturbation ρ_1 obeys (6). Consequently, the exact momentum eq. (10) can be written as

$$\partial_t \boldsymbol{V} + 2\Omega \cos(\theta) \hat{\boldsymbol{z}} \times \boldsymbol{V} = -\frac{1}{\rho_0} \nabla P + \frac{\rho_1}{\rho_0} \boldsymbol{g} + \frac{1}{\rho_0 \mu} B_{0r} \partial_r \boldsymbol{B}$$
$$+ \left[-\boldsymbol{V} \cdot \nabla \boldsymbol{V} + \frac{\tilde{\rho} - \rho_1}{\rho_0} \boldsymbol{g} + \frac{1}{\rho_0 \mu} (\boldsymbol{B} \cdot \nabla \boldsymbol{B} - B_{0r} \partial_r \boldsymbol{B}) \right], \tag{11}$$

where three forcing terms appear in square brackets. The first one, due to Reynolds stresses, is neglected due to the smallness of the Rossby number in Earth's core. The second one is due to thermal anomalies,

$$\boldsymbol{F}_{\text{buoyancy}} = (\tilde{\rho} - \rho_1)\boldsymbol{g}/\rho_0, \tag{12}$$

and the third one to large-scale magnetic stresses,

$$\boldsymbol{F}_{\text{Lorentz}} = (\boldsymbol{B} \cdot \nabla \boldsymbol{B} - B_{0r} \partial_r \boldsymbol{B})/(\rho_0 \mu). \tag{13}$$

Each of the forcing terms in (9), (12) and (13) have two parts. One part depends on the total velocity and magnetic fields, which are mainly due to convection. The second part is a wavelike modification to ensure that the full governing equations are represented. In most previous applications of Lighthill's approach the wavelike corrections are small. We directly verify this approximation for the Lorentz force in eq. (13), which proves to be the largest of the forcing terms.

To be very specific in our subsequent discussion we use overbars to denote properties of the convective state that are unaffected by the waves. These are also the quantities we extract from the dynamo simulations because the wave motion is heavily damped in

the simulation. We stress that $\overline{V}$ and $\overline{B}$ for the total fields are distinct from the background fields V_0 and B_0. The background fields are independent of time and are simply used to obtain linearized wave equations. In the original problem of Lighthill (1952), the overbarred variables would be the turbulent fluctuations that force sound waves, while the background state would simply be at rest. The final expressions of the forcings become

$$F_I = \nabla \times \left(\overline{V} \times \overline{B}\right), \tag{14}$$

$$F_{\text{buoyancy}} = \overline{\rho} g / \rho_0, \tag{15}$$

$$F_{\text{Lorentz}} = \overline{B} \cdot \nabla \overline{B} / (\rho_0 \mu). \tag{16}$$

We now turn to the question of solving the forced wave equations in spherical geometries. Eqs (1)–(6) can be recast into a single scalar equation for the θ component of the magnetic perturbation b_θ (see Appendix A for details). It is convenient to use a modified meridional perturbation $b''_\theta = (1 - y^2) b_\theta$, where $y = \cos(\theta)$ is a modified meridional coordinate. b_θ (and hence b''_θ) is Fourier-transformed in longitude, time and radius. A half-range sine transform is used in the radial direction to most naturally enforce the boundary conditions.[1] Each mode is thus given by

$$b_\theta(t, \lambda, y, z) = \tilde{b}_\theta(y) \sin(kz) e^{i(m\lambda - \omega t)}, \tag{17}$$

where $z = r - R$, m is the angular order, ω the angular frequency and $k = j\pi / H$ with $j > 0$ the radial order. Details of the derivation are similar to Buffett & Matsui (2019) with the addition of forcing terms (see the Appendix). The background radial field B_{0r} is assumed uniform for purposes of analytical tractability. The equation in its final form reads:

$$d_y^2 \tilde{b}''_\theta + \left(\frac{C^2 y^2 + mC}{M(1 - y^2)} - \frac{m^2 - 1}{(1 - y^2)^2}\right) \tilde{b}''_\theta = \mathcal{F}, \tag{18}$$

where C and M are two non-dimensional terms scaling the magnitudes of Coriolis and Lorentz forces relative to buoyancy, given by

$$C = \frac{2\Omega \omega k^2 R^2}{N^2}, \quad M = \frac{B_{0r}^2 k^4 R^2}{\rho_0 \mu \chi N^2} \tag{19}$$

(χ is a magnetic diffusion factor). d_y is the derivation operator for functions that solely depend on y. $\mathcal{F}$ is the sum of five terms that depend linearly on $\tilde{F}_r$, $\tilde{F}_\theta$, $\tilde{F}_\lambda$, $\tilde{F}_{I\theta}$ and $\tilde{F}_{I\lambda}$; later, we assess the wave response to these individual components. The expressions for χ and the forcing term $\mathcal{F}$ are given in the Appendix.

If $|m| \neq 1$, regularity of the solution of eq. (18) imposes that $\tilde{b}''_\theta(y) = \mathcal{O}\left((1 - y^2)^2\right)$, that is $\tilde{b}_\theta(y) = \mathcal{O}\left(1 - y^2\right)$ or equivalently $\tilde{b}_\theta(\pm 1) = 0$. With $|m| = 1$, the $(1 - y^2)^{-2}$ term in the right-hand side of eq. (18) is removed and $\tilde{b}_\theta$ is not required to vanish at the boundaries anymore. However, in order for b_θ to have continuous first derivatives over the poles, one needs $d_y \tilde{b}_\theta(y = \pm 1) = 0$.

2.3 Numerical treatment of the unforced problem

This section details how eq. (18) is solved on a discretized domain in $y = \cos\theta$. Setting $\mathcal{F} = 0$ and multiplying by $-M(1 - y^2)y^{-2}$, the

unforced equation becomes a quadratic eigenvalue problem, where C (or equivalently ω, the wave angular frequency) is the eigenvalue:

$$\left(-\frac{M(1 - y^2)}{y^2} d_y^2 + \frac{M(m^2 - 1)}{y^2(1 - y^2)}\right) \tilde{b}''_\theta - \frac{m}{y^2} C \tilde{b}''_\theta - C^2 \tilde{b}''_\theta = 0. \tag{20}$$

Upon discretization, this problem is converted to a linear eigenvalue problem by defining an extended state vector $\mathbf{x}$ of size $2n$ (where n is the grid size) that is the concatenation of $\tilde{b}''_\theta$ and $C\tilde{b}''_\theta$. This procedure is analogous to casting a second-order differential equation into a first-order equation in the function and its first derivative; $C\tilde{b}''_\theta$ is proportional to the time derivative of $\tilde{b}''_\theta$. $\mathbf{x}$ is solution of

$$\mathbf{Ax} - C\mathbf{x} = 0, \tag{21}$$

where

$$\mathbf{A} = \begin{bmatrix} 0_n & I_n \\ \mathbf{L}_1 & \mathbf{L}_2 \end{bmatrix}, \tag{22}$$

$$\mathbf{L}_1 = -\text{diag}\left(\frac{M(1 - y^2)}{y^2}\right) \mathbf{D}_{2,y} + \text{diag}\left(\frac{M(m^2 - 1)}{y^2(1 - y^2)}\right), \tag{23}$$
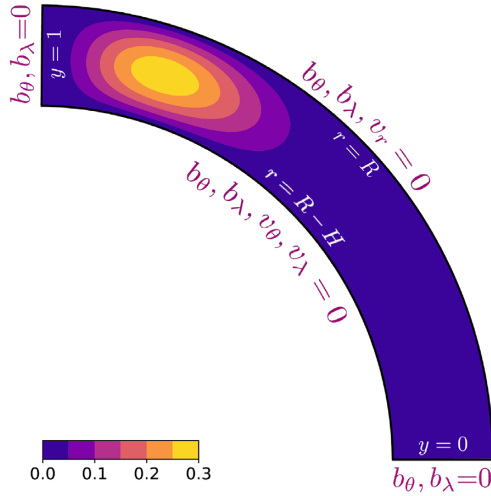
and

$$\mathbf{L}_2 = -\text{diag}\left(\frac{m}{y^2}\right). \tag{24}$$

In (23) and (24), $\text{diag}(f(y))$ denotes an $n \times n$ matrix whose diagonal elements are the values of f on the gridpoints. I_n is the identity matrix of size n. $\mathbf{D}_{2,y}$ is a discrete second derivative on the grid.

The symmetry of the problem with respects to $y = 0$ permits solutions for the modes in one hemisphere only, with $y \in [0, 1]$. Two types of equatorial boundary conditions are considered, depending on the nature of the symmetry. Enforcing $\tilde{b}''_\theta(0) = 0$ gives rise to antisymmetric modes, while $d_y \tilde{b}''_\theta(0) = 0$ yields symmetric modes. Close to the equator, the dominant balance in the unforced version of eq. (18) is $d_y^2 \tilde{b}''_\theta \simeq -mC/M\tilde{b}''_\theta$. With $C < 0$ (westward-travelling modes), $\tilde{b}_\theta$ depends exponentially on y and either boundary condition produces solutions for $\tilde{b}_\theta$ that have very small amplitude in the equatorial region. This leads to high-latitude modes; the symmetric and antisymmetric modes are nearly identical in shape with very similar periods. Henceforth, high-latitude modes will only be solved for with zero boundary conditions at $y = 0$ and $y = 1$. Eastward-travelling waves ($C > 0$) have largest amplitudes at low latitudes. When C is small enough and m is large the $(m^2 - 1)(1 - y^2)^{-2}$ term in eq. (18) dominates at high latitudes, forcing exponential decreases in amplitude toward the poles. Fig. 2 shows the geometry of the wave model and summarizes the boundary conditions.

We solve (21) on a non-uniform grid with $N_y = 150$ points and higher resolution close to the pole, defined by $y_i = \sin\left(\frac{2i - 1}{2N_y} \frac{\pi}{2}\right)$ for $1 \leq i \leq N_y$. Second order derivatives are evaluated using Fornberg's method (Fornberg 1988) with a five-point stencil, giving fourth-order accuracy. Fig. 3 displays the five high-latitude modes ($m = 3$) and five equatorial modes ($m = 6$). In each case the lowest five frequencies are selected. The angular orders were chosen according to the observed SA patterns. Representative values of the core parameters were used, along with $H = 140$ km, $N = 0.5\,\Omega$, $B_{0r} = 0.5$ mT and radial order $j = 1$. (Chi-Durán *et al.* 2020, showed that these values account for the phase speeds of observed waves). The meridional structure and period of the gravest high-latitude mode are consistent with observed waves (see Fig. 1 and Chi-Durán *et al.* 2020); theory predicts westward-travelling modes with periods of about 20 yr, whose amplitude peaks between 65°N and 70°N. Other modes have too much power poleward of 80°N. Using

---

[1] The forcing terms are transformed in the same way, except for F_θ and F_λ whose radial decomposition is a half-range cosine transform, for reasons detailed in the Appendix.

Figure 2. Sketch of the geometry and boundary conditions of the high-latitude wave model. The thickness of the spherical shell has been enlarged for presentation purposes. The amplitude of the gravest high-latitude eigenmode of eq. (20) (period =21.3 yr, westward-travelling) is overlaid.
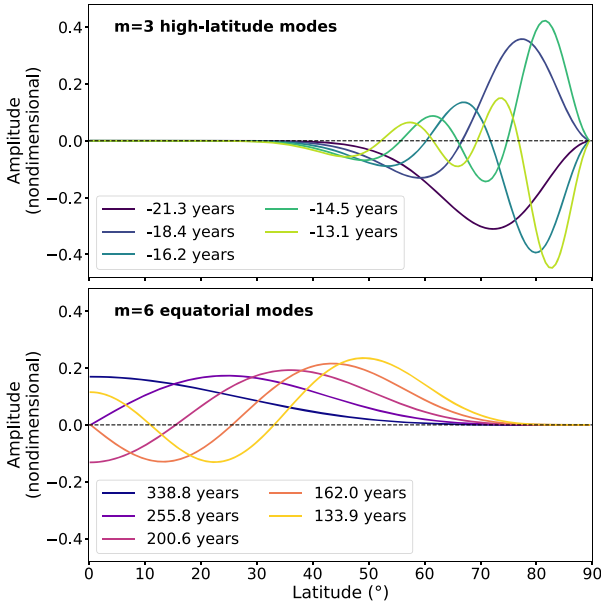
Figure 3. Some eigenmodes of eq. (20) and their associated periods. Westward-travelling (top panel) and eastward-travelling (bottom panel) modes with the longest periods have been selected. Note $\tilde{b}_\theta$, rather than its transformed version, is being plotted.

a realistic background field structure, with decreasing amplitude close to the pole, might alter the structure of the waves above 80°N. Long-period, eastward-travelling equatorial modes are also consistent with observations, although the neglect of meridional variations in the background magnetic field reduces the equatorial confinement (Buffett & Matsui 2019). Relative variations in the amplitude of the background field are less important at high latitudes, justifying the use of a constant B_{0r} in this study.

Note that **A** depends on the damping term χ (through M), which causes the wave frequency, ω, to be complex. Because χ depends on ω we would normally iteratively update χ using the eigenfrequency and repeat the calculations. In practice, we find that waves with decadal periods are lightly damped by magnetic diffusion, so it

suffices to calculate χ using a nominal value of ω. We henceforth use a fixed reference wave period of 20 yr when computing χ.

2.4 Decomposing forced waves on the eigenmode basis

The solutions of eq. (18) for the forced waves can be represented as linear combinations of the eigenmodes of the unforced wave equation. In this subsection, we describe how this decomposition is handled in the discretized version of the wave equation, which reads

$$\mathbf{A}\mathbf{x} - C\mathbf{x} = \mathbf{F}, \tag{25}$$

where **F** is the discretized representation of $-M(1 - y^2)y^{-2}\mathcal{F}$.

We illustrate the idea with the case where **A** has distinct eigenvalues, even though subsequent results are also valid in the more general case where **A** has degenerate eigenvalues (but remains diagonalizable). The sequence of $2n$ eigenvalue-eigenvector pairs of the unforced wave equation is denoted $(C_i, \mathbf{x}_i)$. The eigenvectors $(\mathbf{x}_i)_{i=1..2n}$ form a basis of the discrete space. We seek to express the solutions of eq. (25) as a linear combination of these basis vectors.

Each eigenvalue C_i has an associated left eigenvector, denoted $\mathbf{p}_i$, which satisfies $\mathbf{p}_i^H \mathbf{A} - C_i \mathbf{p}_i^H = 0$, where $(\cdot)^H$ denotes Hermitian conjugation (see e.g. Friedberg *et al.* 2002). Taking the dot product of this identity with $\mathbf{x}_j$, one obtains $\mathbf{p}_i^H \mathbf{A}\mathbf{x}_j - C_i \mathbf{p}_i^H \mathbf{x}_j = 0$. Similarly, $\mathbf{x}_j$ obeys $\mathbf{A}\mathbf{x}_j - C_j \mathbf{x}_j = 0$. Dotting with $\mathbf{p}_i$ (i.e., multiplying by $\mathbf{p}_i^H$ on the left) and subtracting, one obtains

$$\forall i, j, \quad (C_i - C_j)\mathbf{p}_i^H \mathbf{x}_j = 0. \tag{26}$$

Because the eigenvalues are distinct, this gives an orthogonality relationship between left and right eigenvectors. The solution to our forced problem eq. (25) for **x** can thus be decomposed as

$$\mathbf{x} = \sum_{i=1}^{2n} (\mathbf{p}_i^H \mathbf{x})\mathbf{x}_i. \tag{27}$$

Dotting (25) with $\mathbf{p}_i$, one obtains

$$(C_i - C)\mathbf{p}_i^H \mathbf{x} = \mathbf{p}_i^H \mathbf{F}. \tag{28}$$

The solution of the forced problem decomposed on the basis of eigenvectors $(\mathbf{x}_i)$ finally reads:

$$\mathbf{x} = \sum_{i=1}^{2n} \frac{\mathbf{p}_i^H \mathbf{F}}{C_i - C}\mathbf{x}_i. \tag{29}$$

Under this decomposition, forced waves appear as weighted linear combinations of the eigenmodes, with higher weights for the modes whose eigenfrequencies are close to the excitation frequency. Note that eq. (25) could also be solved directly, as a linear system, for each frequency (or equivalently each C). However, eq. (29) is more efficient in that it involves a single 'heavy' computation step (eigendecomposition of **A**), then simple dot products for each different frequency and forcing.

3 ESTIMATION OF SOURCES

Eq. (18) allows two types of forcing terms. One includes terms that arise in momentum equations. The other arises from the forcing term in the induction equation (details are given in the Appendix). Both of these source terms stem from convective motions below the stratified layer. We resort to numerical modelling to estimate their structure.
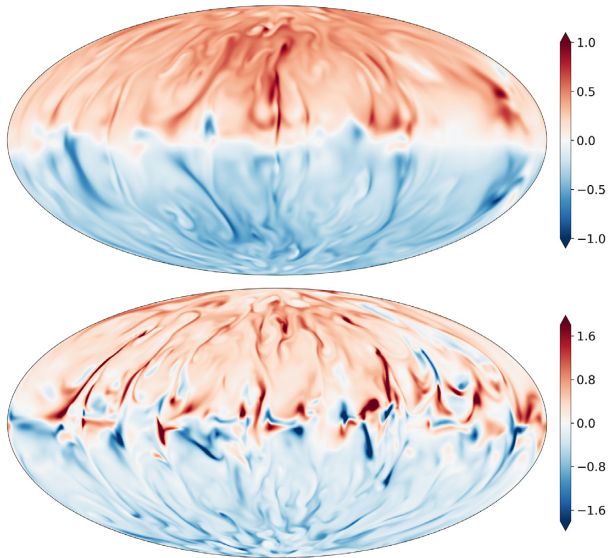
Figure 4. Snapshots of the radial magnetic field at the CMB in the control simulation (top panel) and in the *Pm* = 2 simulation (bottom panel), in Elsasser units (i.e. we represent $B/(\sqrt{\rho\mu\Omega\eta})$). An Aitoff projection is used.

We employ the geodynamo model *Calypso* (Matsui *et al.* 2014) to constrain the spatial structure and time dependence of the forcing terms. *Calypso* solves the magnetohydrodynamics equations under the Boussinesq approximation in a rotating fluid shell with Earth's core geometry. Uniform temperatures are imposed at the CMB and inner core boundary (ICB) to drive convection. Equations are non-dimensionalized using the diffusion-free scaling of Christensen & Aubert (2006). In addition to boundary conditions and a heat sink (see below), four parameters specify a given model run:

$$E = \frac{\nu}{\Omega L^2}, \quad Pr = \frac{\nu}{\kappa}, \quad Pm = \frac{\nu}{\eta}, \quad Ra^* = \frac{\alpha_T g \Delta T}{\Omega^2 L}, \tag{30}$$

where ν is the fluid's dynamic viscosity, κ its thermal diffusivity, α_T its coefficient of thermal expansion, ΔT the temperature gap across the outer core and $L = 0.65R$ the outer core thickness, hereafter 2260 km. We recall that g is defined as the acceleration of gravity at the CMB. Fields are represented using spherical harmonics, with a triangular truncation at degree $l_{\max} = 255$. The radial grid consists of 360 Chebyshev collocation points, which translates into a maximum radial grid spacing of 10 km and a mean grid spacing of 2 km within 150 km of the boundaries.

Source terms are extracted from a control run with parameters $E = 10^{-5}$, $Pr = 1$, $Pm = 0.5$ and $Ra^* = 3200$. The magnetic Reynolds number (*Rm*) for this run is approximately 200. In order to reach more robust conclusions, we run a second simulation with the same parameters, except $Pm = 2$. This has the effect of lowering magnetic diffusivity, increasing *Rm* to 900, that is closer to expected values in Earth's core. Snapshots of the radial magnetic field at the CMB in both runs are shown in Fig. 4, at full resolution. The field is predominantly dipolar and has a more heterogeneous structure in the $Pm = 2$ simulation, with more reversed flux patches present in both hemispheres.

MAC waves are not supported in simulations with the stated parameters because of the strong damping due to viscosity (*E* is 10 orders of magnitude bigger than in Earth's core) and due to magnetic diffusion ($E_\eta := E/Pm$ is four orders of magnitude too big). One way to quantify the damping of waves is in terms of the quality factor $Q = \Re(\omega)/(2\Im(\omega))$. For high-latitude waves of period $\mathcal{O}(10)$

years the quality factor is roughly 50 at Earth's core conditions. With model parameter values (and stratified layer characteristics), calculations show that the waves are critically damped, precluding their detection. Two other quantities characterizing the presence of hydromagnetic waves in such simulations are the Lundquist number $S = \tau_\eta/\tau_A$ and the Alfvén number $A = \tau_A/\tau_U$, where $\tau_A = L\sqrt{\rho_0\mu}/B$, $\tau_\eta = L^2/\eta$ and $\tau_U = L/U$ are, respectively, the Alfvén, magnetic diffusion, and core overturn timescales. The control simulation has $S = 350$ while the $Pm = 2$ simulation has $S = 1700$, above the value of 900 suggested by Aubert & Gillet (2021) for the presence of waves in a dynamo simulation. However, the Alfvén number in these runs is, respectively, 0.6 and 0.5, which is not small enough to separate waves from the convective background. Aubert & Finlay (2019) showed that lowering diffusivities in a suite of geodynamo models towards Earth's core conditions allows the emergence of rapid Alfvén waves resembling observed equatorial oscillations. This supports the idea that the MAC waves studied herein could be generated by the model, if more realistic parameter values (lower *E* and *Pm*) were used.

Although the model is not expected to support MAC waves, the presence of a stratified layer is required to support the waves. This means we want to account for stratification in assessing the magnitude of the source terms due to the underlying convection. Applying a uniform heat sink through the volume of the core lowers the heat flow at the CMB. When the integrated heat sink exceeds the ICB heat flow we expect an inflow of heat at the CMB, which establishes a thermally stratified layer. We use the same heat sink amplitude as Buffett & Knezek (2018), yielding a stratified layer of thickness 290 km with a buoyancy frequency $N \simeq 0.14\Omega$.

Accurate estimation of MAC wave amplitudes in Earth's core requires the sources to have the correct spatial and temporal patterns. Aubert *et al.* (2017) show that the spatial scales of convection in dynamo models become asymptotically invariant once a force balance between pressure, Coriolis, Lorentz and buoyancy forces (the QG-MAC balance) is established at large scales. One way to assess whether our model is close to a QG-MAC balance is to evaluate the extent to which magnetic energy exceeds kinetic energy (Schwaiger *et al.* 2019). In our calculations the ratio of magnetic to kinetic energy is between 2.5 (control run) and 4 (*Pm* = 2 run), giving support that our model sits in a QG-MAC balance and accurately captures the large spatial scales of convection.

The temporal scale of sources depends on the way we choose to dimensionalize model outputs. Once the spatial scales are reasonable we require suitable estimates for the dimensional velocities to obtain the correct temporal dependencies. Because velocities are scaled by ΩL (and L is fixed to the actual core value), one needs to choose an appropriate rotation rate Ω to convert from model time to dimensional time. The Rossby number in our simulation is $Ro = U/(\Omega L) \simeq 4 \times 10^{-3}$, and realistic estimates of the core velocities are on the order of 4×10^{-4} m s^{-1}. A modified rotation rate $\Omega_{\text{adjusted}} = 4.4 \times 10^{-8}$ s^{-1} gives dimensional model velocities in the expected range. Model outputs are reported at a non-dimensional time interval of 0.25. This corresponds to a dimensional time interval of 66 d, which is sufficient to resolve the excitation of a 20-yr wave. The duration of both simulations is 800 time units, that is 144 yr, or about one core overturn time. In the range of frequencies resolved by the model, various magnetic field components are expected to follow a power law of the form $P \propto \omega^{-4}$, with ω the frequency (Bouligand *et al.* 2016). We verified (not shown) that the temporal spectrum of the field's dipole component conforms to this law in our dynamo model at high frequencies.

While the Lorentz force is directly output by the model, the two other forcings require additional processing. For buoyancy, we extract the temperature field T and write $\boldsymbol{F}_{\text{buoyancy}} = \tilde{\overline{\rho}}\boldsymbol{g}/\rho_0 = -\alpha_T \overline{T}\boldsymbol{g}$. For the large-scale induction term, we exploit the fact that the magnetic Reynolds number is high ($Rm \geq 200$) to write $\nabla \times (\overline{\boldsymbol{V}} \times \overline{\boldsymbol{B}}) \simeq \partial_t \overline{\boldsymbol{B}}$. Hence, we extract the magnetic field $\overline{\boldsymbol{B}}$ from the model and apply the time derivative in the Fourier domain $\tilde{\boldsymbol{F}}_I = -i\omega \tilde{\overline{\boldsymbol{B}}}$.

To further illustrate the scales of convection in the dynamo model, we show equatorial and meridional cross-sections of instantaneous temperature anomalies from the control run in Fig. 5. The equatorial pattern is dominated by hot plumes rising from the ICB. The scale and structure of these plumes are similar to simulations carried at much lower E (see fig. 6 in Aubert *et al.* 2017). It is expected that large-scale structures become invariant in the asymptotic QG-MAC regime. Reduced thermal anomalies near the CMB are a consequence of thermal stratification in the simulation. Weaker anomalies penetrate into the base of the stratified layer, which is denoted by the thin dashed line and sits 290 km below the CMB in the model. These anomalies carry buoyancy fluctuations that can generate MAC waves through the F_r term in eq. (18). Because we expect waves to be mostly forced by the large-scale structures, the fact that these structures are similar to more realistic models gives confidence in the accuracy of our approach. The meridional section shows that temperature anomalies are organized in axially columnar structures, as expected from the Taylor–Proudman constraint. Buoyant material is mostly contained close to the equator and within the tangent cylinder. The concentration of light fluid close to the equator is compensated by the presence of denser material below the CMB at high latitudes, creating stronger stratification there. We note that this meridional gradient in stratification is not taken into account in our wave model.

4 COMPARING INFERRED WAVES TO THE OBSERVED GEOMAGNETIC ACCELERATION

The forced MAC wave eq. (18) is solved using source terms computed from the dynamo simulations. The dynamo calculations are scaled to achieve realistic spatial and temporal properties (see Section 3). However, upon dimensionalization, the amplitude of the sources differs from expectations in the core. For example, using the value of Ra^* from the simulations along with realistic values for α_T, g and L and the chosen scale Ω_{adjusted} yields a temperature jump across the core of 0.1 K, an order of magnitude above current estimates (King *et al.* 2010). In order to recover reasonable amplitudes for the waves we need to extrapolate the forcing terms from the dynamo model to Earth-like conditions in the core.

There are several ways the extrapolation can be done. We might use scaling laws (e.g. Davidson 2013) to adjust the dynamo solution to make predictions for what would have been computed if we could use realistic parameters in the calculations. Often these scaling laws are tested by showing that the extrapolations produce dimensional quantities that are consistent with expectations at Earth's core conditions (e.g. Aubert *et al.* 2017). Alternatively, we could use differences between the model output and expectations to adjust the source terms. The discrepancy noted above for the temperature drop across the core is an example. We adopt the second approach here because it avoids the need to introduce a specific scaling law.

4.1 Dimensionalization and extrapolation of the simulated forcing terms

The various quantities extracted from the dynamo model to serve as forcings are non-dimensional, and need to be scaled appropriately before being used alongside the dimensional, Earth-like quantities in the left-hand side of (18). Denote one generic Fourier component of a non-dimensional source term by $\tilde{S}^*_{m,j,\omega^*}(y)$, recalling that m is the spherical order, j the radial order and ω^* the non-dimensional frequency. Its dimensional counterpart is $\tilde{S}_{m,j,\omega}(y) = \mathcal{S}\tilde{S}^*_{m,j,\omega/\Omega_{\text{adjusted}}}(y)$, where $\mathcal{S}$ is a dimensional scaling factor and we recall that time is scaled with an adjusted rotation rate to achieve realistic temporal dependencies. The form of $\mathcal{S}$ for each forcing term is known from the characteristic scales used in the dynamo model. When we use realistic physical properties (ρ_0, μ, g, α_T, L) and our adjusted rotation rate to evaluate terms in $\mathcal{S}$ we are lead to inconsistencies, stemming from the fact that the dynamo model does not sit in a realistic parameter space. Adjustments to the sources are used to eliminate these inconsistencies.

We illustrate using the buoyancy force from Section 3. The dimensional form of the buoyancy force is

$$\boldsymbol{F}_{\text{buoyancy}} = -\alpha_T \overline{T}\boldsymbol{g} = -\alpha_T \Delta T \overline{T}^*\boldsymbol{g}. \tag{31}$$

The temperature scale in the dynamo model corresponds to the change in temperature across the core. We recover an estimate of the temperature jump from the simulations

$$\Delta T = Ra^* \Omega^2_{\text{adjusted}} L/(\alpha_T g) \simeq 0.13 \text{ K},$$

where we have used realistic values for α_T and g. Because our estimates for the actual temperature jump are lower ($\Delta T = 10$ mK, King *et al.* 2010), we scale $\boldsymbol{F}_{\text{buoyancy}}$ by 0.076 to achieve a more realistic source amplitude.

The dimensional Lorentz force is given by

$$\boldsymbol{F}_{\text{Lorentz}} = \overline{\boldsymbol{B}} \cdot \nabla \overline{\boldsymbol{B}}/(\rho_0 \mu) = (\Omega^2_{\text{adjusted}} L)\overline{\boldsymbol{B}}^* \cdot \nabla^* \overline{\boldsymbol{B}}^*. \tag{32}$$

With this scaling, the simulated root-mean-square magnetic field is

$$B_{\text{sim.,RMS}} = \sqrt{\rho_0 \mu}\Omega_{\text{adjusted}} L |\overline{\boldsymbol{B}}^*| \simeq 0.078 \text{ mT}$$

in the control run (0.093 mT in the $Pm = 2$ run), whereas a representative $B_{\text{Earth, RMS}}$ inside the core is 4 mT (Gillet *et al.* 2010). Henceforth, $\boldsymbol{F}_{\text{Lorentz}}$ is scaled by a factor $B^2_{\text{Earth,RMS}}/B^2_{\text{sim.,RMS}} = 2630$ (1850 in the $Pm = 2$ run) to correct for this underestimation. Note we have assumed that the characteristic length for magnetic field gradients inside the core is adequately represented by the model (as described in Section 3).

Finally, the dimensional induction source term is given by

$$\boldsymbol{F}_I = \partial_t \overline{\boldsymbol{B}} = \Omega_{\text{adjusted}}(\sqrt{\rho_0 \mu}\Omega_{\text{adjusted}} L)\partial_{t^*}\overline{\boldsymbol{B}}^*. \tag{33}$$

For the same reason as the Lorentz term, this underestimates the realistic amplitude by a factor $B_{\text{sim., RMS}}/B_{\text{Earth, RMS}}$. Hence, $\boldsymbol{F}_I$ is subsequently scaled by a factor $B_{\text{Earth, RMS}}/B_{\text{sim., RMS}} = 51$ for the control run and 43 for the $Pm = 2$ run.

We now use these expressions to compute forced MAC waves at wide temporal and spatial scales.

4.2 Exciting MAC waves with a wide range of frequencies and spatial structures

Because the observed high-latitude waves have primarily an azimuthal order $m \simeq 3$ (see Fig. 1), we will only consider forcings
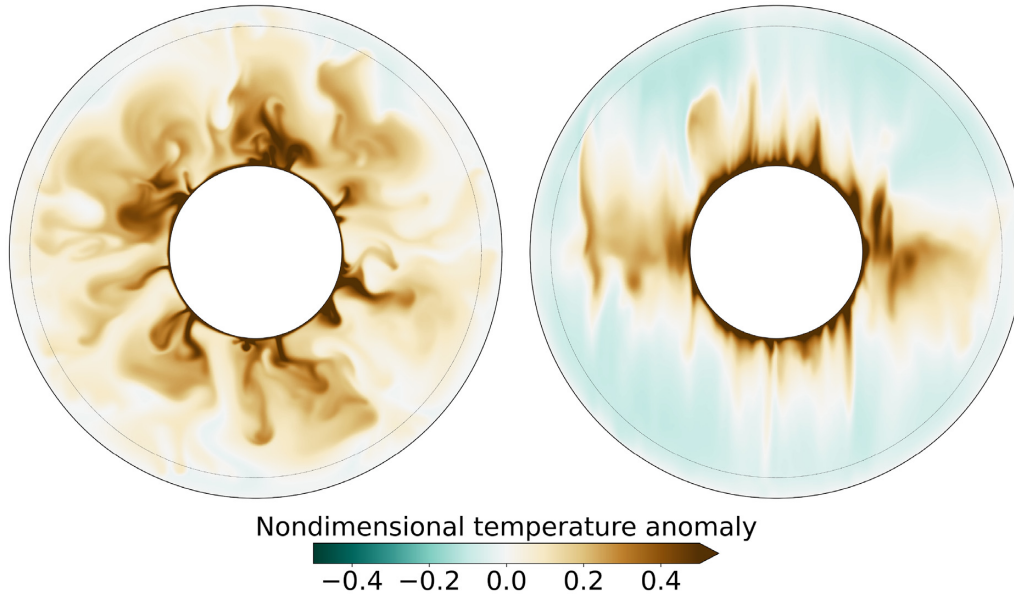
Figure 5. Snapshots of instantaneous temperature fluctuations from the control run in the equatorial plane (left-hand panel) and a meridional plane (right-hand panel). Note that the colourscale has been saturated to better render convective plumes; temperature anomalies are unity at the ICB.

and waves of order $m = 3$. The relevant quantities from the dynamo model at $m = 3$ ($\overline{T}^*$, $\overline{\boldsymbol{B}}^* \cdot \nabla^* \overline{\boldsymbol{B}}^*$, $\overline{\boldsymbol{B}}^*$) are first interpolated onto a spherical grid containing 300 meridional points from the South Pole to the North Pole (using the Chebyshev grid layed out in Section 2.3, extended to both hemispheres) and a uniform radial grid containing 58 points in the stratified layer (the number of radial gridpoints is equal to the number of radial Chebyshev gridpoint employed by *Calypso* in the same radial interval). The meridional resolution was chosen as a compromise between adequate resolution of the modes and ease of computation. Vector quantities are also converted from a toroidal-poloidal representation to spherical (r, θ, λ) components. Each forcing is then Fourier-transformed in time and in the radial dimension, yielding a function of radial order j, non-dimensional frequency ω^* and meridional coordinate y. These quantities are converted to dimensional form and extrapolated as laid out in Section 4.1, yielding Earth-like forcing terms. The first radial order is observed to account for over 90 per cent of the wave forcing, so we only consider $j = 1$ modes. For each separate forcing, we compute a wave spectrum $\tilde{b}_\theta(\omega, y)$ using expression (29). From such a spectrum, one can then compute a meridionally resolved RMS value $b_{\theta, tRMS}(y)$ using Parseval's relation, as well as a power spectrum $|\tilde{b}_{\theta, yRMS}(\omega)|^2$ by taking the RMS over the y dimension. As explained in Section 2.3, waves are solved for on one hemisphere only: we split the Northern and Southern Hemisphere parts of each forcing and average the power of the waves excited by each part.

The high-latitude y-RMS power spectrum $|\tilde{b}_{\theta, yRMS}(\omega)|^2$ (the RMS has been computed over latitudes poleward of $45°$) is displayed in Fig. 6, left-hand panels. Lorentz forces and induction prove to be the strongest excitation sources, with similar peak magnitudes at small eastward-travelling frequencies. All three components of the Lorentz force have similar magnitudes, but they do not excite equal amplitude waves. The reason is due to the geometry of the waves. The aspect ratio of horizontal to radial length scales is 10^2. This geometry means that a hydrostatic force balance is dominant in the radial direction and the radial forcings contribute less to the wave generation. Forcings in the horizontal direction are much more efficient at exciting waves [as the factor $(Rk)^{-1}$ attests in eq. (18)].

With a higher temporal discretization, one should expect to see distinct peaks around the eigenfrequencies of the wave operator. However, the frequency range shown in Fig. 6 is populated with closely spaced eigenfrequencies that preclude any such peaks. Even though the amplitude of the waves is averaged over high latitudes, eastward-travelling ($\omega > 0$) modes have significant power, comparable even to westward-travelling modes. Indeed, although these eastward modes are associated with equatorially focused structures (see Section 2.3), they can have important power in high latitudes, especially at lower m. Beyond the interval containing the eigenfrequencies (not shown), one observes a sharper decrease in the spectrum [proportional to $F(\omega)/\omega^2$, as expected from (29)].

The time-RMS $b_{\theta, tRMS}(y)$ is shown on the right-hand panels of Fig. 6. Most of the wave power is contained at high latitudes. This is expected because westward-travelling (high-latitude) waves are confined to the polar region, whereas the eastward-travelling waves have power at high and low latitudes (see Fig. 3 and Section 2.3). Had we accounted for meridional gradients in the background field, eastward-propagating waves would have shown more equatorial confinement Buffett & Matsui (2019). The resulting wave power at the equator would have been higher, in line with observations (e.g. Chulliat *et al.* 2010; Chulliat & Maus 2014). We note that these RMS patterns have significant power at latitudes poleward of $80°$, unlike observations (Fig. 1). This power is dominated by high-frequency signals with small-scale spatial variations that are undetectable at the Earth's surface. Only the structure of the graver modes with broad spatial structures (shown in Fig. 3) are relevant to the comparison with observations.

4.3 Exciting westward-travelling waves with a 20-yr period

This study was originally motivated by the observation of high-latitude waves travelling westward with a 20-yr period (see Fig. 1). In this section, we investigate whether MAC waves of similar amplitude could plausibly be generated inside the core. The 20-yr westward frequency is shown in Fig. 6 as a dashed black line. The meridional magnetic perturbation carried by waves excited at
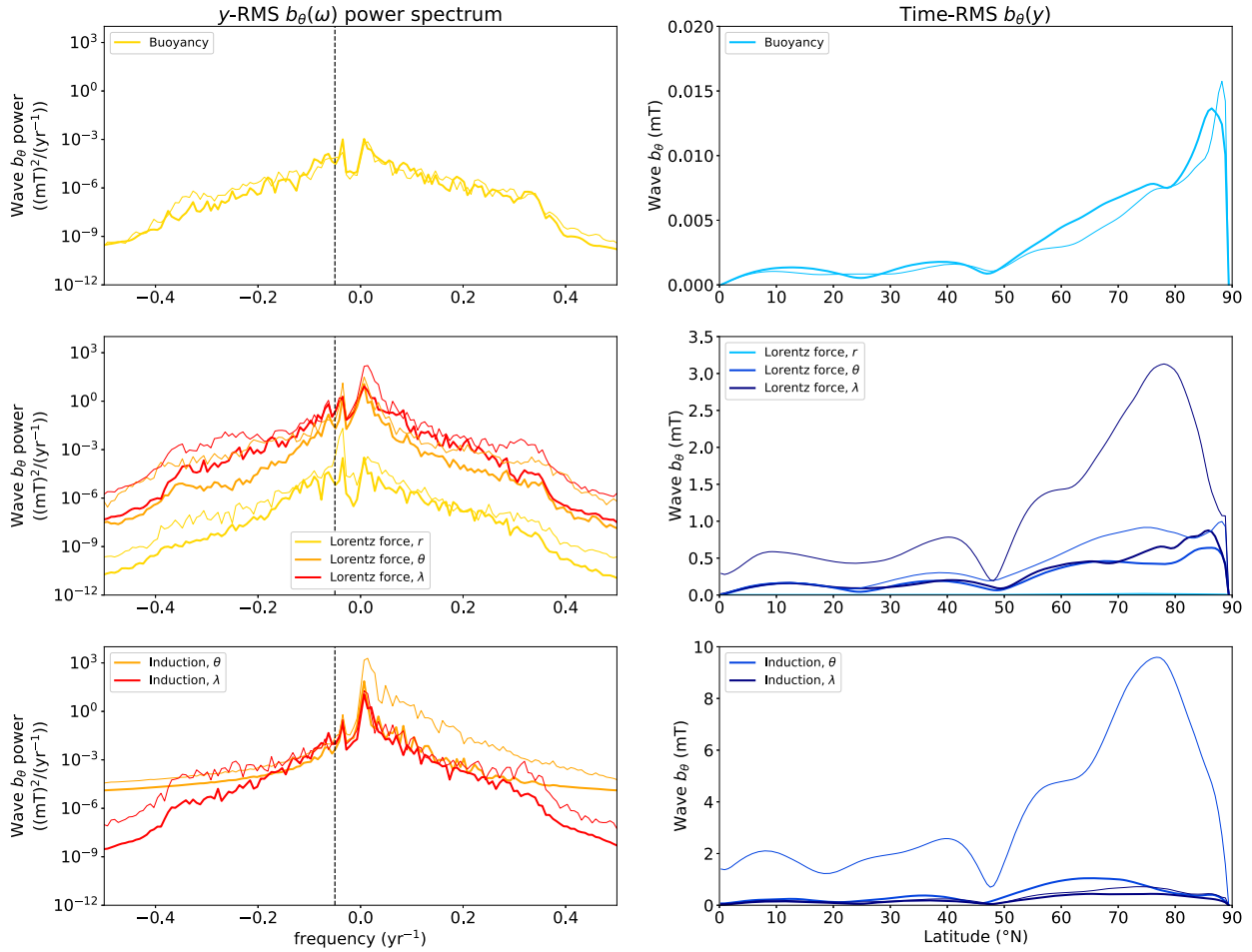
Figure 6. Predicted wave geomagnetic acceleration at the top of Earth's core, with three different source terms. Left-hand panel: power spectra, RMS over latitudes poleward of 45°. Right-hand panel: RMS over all frequencies, as a function of latitude. Top, middle and bottom rows, respectively, show waves forced by thermal, Lorentz and induction sources. Thick (thin) lines correspond to waves forced by the control (Pm=2) simulation.

this frequency, when integrated over a frequency interval of width $0.007\ \mathrm{yr}^{-1}$ (an approximately 3-yr period interval) and averaged over latitudes poleward of 45°, is $b_\theta = 4.6 \times 10^{-4}$, 4.4×10^{-2} and 1.0×10^{-2} mT for waves forced by buoyancy, Lorentz force and induction, respectively, from the control simulation. Using forcings from the *Pm* = 2 simulation, these values go up by 57, 13 and 47 per cent. We now relate this meridional magnetic perturbation to a SA $\ddot{b}_r$ to facilitate comparison with observations.

High *Rm* in the core suggests that the radial induction equation can be approximated by

$$\dot{b}_r = [\nabla \times (\boldsymbol{v} \times \boldsymbol{B})]_r = -\nabla_H \cdot (\boldsymbol{v}_H B_{0r}), \tag{34}$$

where the subscript H denotes the horizontal projection of a 3-D vector. Although we neglected the influence of gradients in the background magnetic field B_{0r} in deriving the wave eq. (18), we consider their effects again here. Indeed, while the wave dynamics are influenced by the full structure of the magnetic field [even small scale components that cannot be observed, justifying the use of a constant RMS value for B_{0r} in eq. (18)], only the long wavelength parts contribute to the observed SA, which depends more strongly on their spatial structure. We differentiate eq. (34) in time, noting that the wave timescale is much shorter than the secular variation time:

$$\ddot{b}_r \approx \nabla_H \cdot (\dot{\boldsymbol{v}}_H B_{0r}). \tag{35}$$

We finally obtain an order of magnitude for the right-hand side as $|\dot{v}_\theta| B_{0r}/L_B$, where L_B is the horizontal length scale of variations in B_{0r}. Note this estimate assumes that the horizontal divergence of the wave velocity is small compared to $|v_\theta|/L_B$, which is reasonable with a small aspect ratio and in the presence of stratification. Using the induction equation to relate b_θ and v_θ, we obtain $\ddot{b}_r = 0.0024$, 0.22 and 0.051 $\mu\mathrm{T}\ \mathrm{yr}^{-2}$ for waves forced by buoyancy, Lorentz force and induction, respectively. These values again increase by 57, 13 and 47 per cent using sources from the *Pm* = 2 run.

Hence, Lorentz forces are the largest generation mechanism for high-latitude MAC waves with decadal periods. We note that the hierarchy of excitation sources, as well as the amplitude of the forced waves, stay unchanged with different convective morphologies (control and *Pm* = 2 runs). While the amplitude estimate is about an order of magnitude below observations (Fig. 1), it comes after a number of approximations, most notably in the extrapolation of the amplitudes of the various forcing terms to Earth-like conditions. Although the small time span and sensitivity of current observations limit the detection to a single wave mode, it is reasonable to expect more features to become observable in the future with longer coverage. From Fig. 6, one would expect higher-amplitude, longer period waves and lower amplitude, shorter period waves to complement the observed high-latitude 20-yr signal. For waves forced by magnetic stresses, the present framework predicts 10-yr

waves with SA amplitudes $\ddot{b}_r = 0.12\,\mu\text{T}\,\text{yr}^{-2}$ and 40-yr waves with $\ddot{b}_r = 0.80\,\mu\text{T}\,\text{yr}^{-2}$.

Three main factors influence the above-mentioned estimates: the sources, the wave model and the frequency interval over which the wave amplitude is integrated. The latter has been chosen somewhat arbitrarily and longer observations times may allow to resolve wave spectra to provide direct comparison with the present result. Beyond reasonable assumptions such as linearization, the use of a constant background field, or Lighthill's approximation, the wave model is especially sensitive to the size H and strength N of the stratified layer. The values presently used ($H = 140$ km and $N = 0.5\Omega$) are in the low end of the range of values proposed in past literature (Gastine *et al.* 2020). Allowing for stronger stratification would shift wave power towards higher frequencies, while deepening the layer would generally increase wave amplitudes. Finally, uncertainties in the strengths of forcings are both intrinsic to the dynamo model and stem from the assumptions made when extrapolating model amplitudes to Earth-like conditions. Changes in the spatial distribution of some forcings could happen closer to Earth's core conditions. For example, Schaeffer *et al.* (2017) showed that the strength of the magnetic field increased inside the tangent cylinder in low-diffusivity, high-resolution simulations of Earth's core. This could increase the strength of the Lorentz force at high latitudes. We also assumed that the temporal spectrum of sources was accurately simulated once the core overturn time was set to a realistic value (see Section 3). Aubert & Gillet (2021) observed an increase in the power of magnetic acceleration energy at decadal frequencies in a suite of large eddy simulations nearing Earth's core conditions. Such an effect could also increase forced wave amplitudes. The length of our integrations (144 yr) is relatively short compared to the period of the waves, and a different sample could conceivably have more power in the convective excitation. As for the amplitude extrapolation, one could consider dropping the assumption of fixed convective length scales. Allowing, for example length scales to decrease slowly as $E^{1/9}$ (Davidson 2013; Aubert *et al.* 2017), the strength of the Lorentz source would be increased by an order of magnitude, yielding higher wave amplitudes. This change is large enough to bring the amplitude of excited waves in line with observational estimates.

We conclude this section by coming back to the observed pattern of geomagnetic acceleration (Fig. 1). The magnetic acceleration patches are associated with secular variation patches, which Livermore *et al.* (2017) interpreted as the signature of a high-latitude zonal jet, located close to the tangent cylinder, acting on azimuthal gradients in the field. The hemispheric confinement of the jet would explain the observed asymmetry: SA patches are stronger between 90°E and 270°E. We note that this interpretation does not account for the fast westward drift of the SA pattern, and that Gillet *et al.* (2019) later suggested that Livermore *et al.* (2017) had overestimated the acceleration of this jet. In our interpretation, the tangent cylinder plays no role in setting the position of the SA patches: it is a consequence of the structure of the modes, as we illustrate in Fig. 7. Our explanation for these SA patches also relies on flow acting on background field gradients. In our case the flow is due solely to a MAC wave. Unlike the zonal jet interpretation, flow velocities in a $m = 3$ MAC wave are hemispherically symmetric. Still, field gradients are stronger where the SA patches are present, which could explain the asymmetry seen in observations. Alternatively, a hemispherically confined forcing could excite a $m = 1$ MAC wave that would superimpose on the $m = 3$ signal and produce the asymmetry. Another peculiarity of the observed signal is the absence of
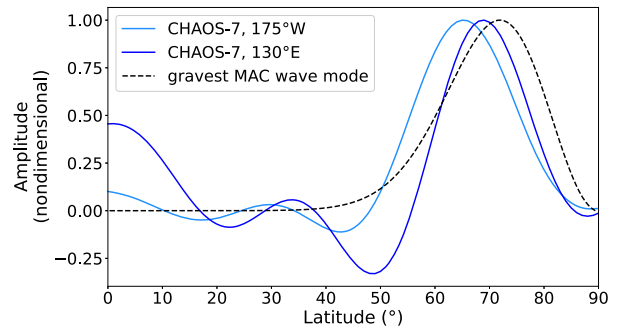
Figure 7. Comparison of meridional structures in observed secular acceleration and in the MAC wave model. The solid blue lines are meridional sections of the CHAOS-7.12 geomagnetic acceleration at the longitudes of two high-latitude patches (truncated at degree $l = 13$; see Fig. 1), normalized by their extremal value. The dashed black line shows the gravest high-latitude eigenmode (period $= 21.3$ yr) displayed in Fig. 3, also normalized.

corresponding SA patches in the Southern Hemisphere. This is easily explained in our interpretation by the decoupling of Northern and Southern Hemisphere modes (see Section 2.3). While one may expect the Taylor–Proudman constraint to correlate forcings between the two hemispheres, this cannot happen within the tangent cylinder. Accordingly, we find little correlation between forcings in the Northern and Southern high latitudes in our dynamo model. The smallness of background field gradients in the South would also explain why the signature of waves in the SA pattern is muted.

5 CONCLUSION

Recent geomagnetic observations reveal waves propagating at high latitudes with decadal frequencies. Several explanations have been advanced for their equatorial counterparts, both with stratification (equatorial MAC waves) and without (non-axisymmetric Alfvén waves and high frequency MC waves), but few have been proposed in the context of high-latitude waves to date. We examine the plausibility of MAC wave generation at these latitudes by various convection-related processes: buoyancy, Lorentz forces and induction. We first derive a unified physical model for MAC waves that retains full spherical geometry and includes generic forcing terms from both the momentum and induction equations. We introduce a method to solve for forced waves by projecting the sources on the adjoint eigenmodes of the unforced equation. Buoyancy, Lorentz and induction forcings are then estimated from a dynamo model. We extrapolate their strength from the parameter space in which the model sits to Earth's core conditions, assuming that the characteristic length scale of convective structures is accurately captured by the model (an assumption that is supported by MAC balance theory).

Bringing dynamo-extrapolated sources into the forced MAC wave equation allows to retrieve full wave spectra, including eastward-travelling and westward-travelling waves from monthly to centennial frequencies. Westward-travelling modes at decadal frequencies have meridional structures consistent with observed high-latitude patterns. At these frequencies, magnetic stresses prove to excite waves most efficiently, yielding an amplitude of $\ddot{b}_r = 0.25\,\mu\text{T}\,\text{yr}^{-2}$ for 20-yr waves. This estimate is within an order

of magnitude of the observations despite the numerous approximations made in obtaining it. The present model requires modest stratification and stratified layer depth, highlighting convection-generated MAC waves as a credible candidate for observed high-latitude oscillations.

ACKNOWLEDGMENTS

DATA AVAILABILITY

Processed model output and the code used in solving for forced and unforced MAC waves are archived at Zenodo (Nicolas 2023a, b). The CHAOS7 model is available at http://www.spacecenter.dk/files/magnetic-models/CHAOS-7/, and was processed using the ChaosMagPy package (Kloss 2022).

REFERENCES

Aubert, J. & Finlay, C.C., 2019. Geomagnetic jerks and rapid hydromagnetic waves focusing at Earth's core surface, *Nat. Geosci.,* **12**(5), 393–398.

Aubert, J. & Gillet, N., 2021. The interplay of fast waves and slow convection in geodynamo simulations nearing Earth's core conditions, *J. geophys. Int.,* **225**(3), 1854–1873.

Aubert, J., Gastine, T. & Fournier, A., 2017. Spherical convective dynamos in the rapidly rotating asymptotic regime, *J. Fluid Mech.,* **813**, 558–593.

Bloxham, J., 1992. The steady part of the secular variation of the Earth's magnetic field, *J. geophys. Res.,* **97**(B13), 19 565–19 579.

Bouligand, C., Gillet, N., Jault, D., Schaeffer, N., Fournier, A. & Aubert, J., 2016. Frequency spectrum of the geomagnetic field harmonic coefficients from dynamo simulations, *J. geophys. Int.,* **207**(2), 1142–1157.

Braginsky, S.I., 1993. MAC-oscillations of the hidden ocean of the core, *J. Geomagnet. Geoelectr.,* **45**(11–12), 1517–1538.

Braginsky, S.I., 1998. Magnetic Rossby waves in the stratified ocean of the core, and topographic core-mantle coupling, *Earth, Planets Space,* **50**(8), 641–649.

Buffett, B., 2014. Geomagnetic fluctuations reveal stable stratification at the top of the Earth's core, *Nature,* **507**(7493), 484–487.

Buffett, B. & Knezek, N., 2018. Stochastic generation of MAC waves and implications for convection in Earth's core, *J. geophys. Int.,* **212**(3), 1523–1535.

Buffett, B. & Matsui, H., 2019. Equatorially trapped waves in Earth's core, *J. geophys. Int.,* **218**(2), 1210–1225.

Chi-Durán, R., Avery, M.S., Knezek, N. & Buffett, B.A., 2020. Decomposition of geomagnetic secular acceleration into traveling waves using complex empirical orthogonal functions, *Geophys. Res. Lett.,* **47**(17), e2020GL087940 , doi:10.1029/2020GL087940.

Chi-Durán, R., Avery, M.S. & Buffett, B.A., 2021. Signatures of high-latitude waves in observations of geomagnetic acceleration, *Geophys. Res. Lett.,* **48**(20), e2021GL094692, doi:10.1029/2021GL094692.

Christensen, U.R. & Aubert, J., 2006. Scaling properties of convection-driven dynamos in rotating spherical shells and application to planetary magnetic fields, *J. geophys. Int.,* **166**(1), 97–114.

Chulliat, A. & Maus, S., 2014. Geomagnetic secular acceleration, jerks, and a localized standing wave at the core surface from 2000 to 2010, *J. geophys. Res.,* **119**(3), 1531–1543.

Chulliat, A., Thébault, E. & Hulot, G., 2010. Core field acceleration pulse as a common cause of the 2003 and 2007 geomagnetic jerks, *Geophys. Res. Lett.,* **37**(7) , doi:10.1029/2009GL042019.

Davidson, P.A., 2013. Scaling laws for planetary dynamos, *J. geophys. Int.,* **195**(1), 67–74.

Finlay, C.C., Kloss, C., Olsen, N., Hammer, M.D., Tøffner-Clausen, L., Grayver, A. & Kuvshinov, A., 2020. The CHAOS-7 geomagnetic field model and observed changes in the South Atlantic anomaly, *Earth, Planets Space,* **72**(1), doi:10.1186/s40623-020-01252-9.

Fornberg, B., 1988. Generation of finite difference formulas on arbitrarily spaced grids, *Math. Comput.,* **51**(184), 699–706.

Friedberg, S.H., Insel, A.J. & Spence, L.E., 2002. *Linear Algebra,* 4th edn, Prentice Hall.

Friis-Christensen, E., Lühr, H. & Hulot, G., 2006. Swarm: a constellation to study the Earth's magnetic field, *Earth, Planets Space,* **58**(4), 351–358.

Gastine, T., Aubert, J. & Fournier, A., 2020. Dynamo-based limit to the extent of a stable layer atop Earth's core, *J. geophys. Int.,* **222**(2), 1433–1448.

Gerick, F., Jault, D. & Noir, J., 2021. Fast quasi-geostrophic magneto-Coriolis modes in the Earth's core, *Geophys. Res. Lett.,* **48**(4), e2020GL090803 , doi:10.1029/2020GL090803.

Gillet, N., Jault, D., Canet, E. & Fournier, A., 2010. Fast torsional waves and strong magnetic field within the Earth's core, *Nature,* **465**(7294), 74–77.

Gillet, N., Huder, L. & Aubert, J., 2019. A reduced stochastic model of core surface dynamics based on geodynamo simulations, *J. geophys. Int.,* **219**(1), 522–539.

Gillet, N., Gerick, F., Angappan, R. & Jault, D., 2022. A dynamical prospective on interannual geomagnetic field changes, *Surv. Geophys.,* **43**(1), 71–105.

Hori, K., Jones, C.A. & Teed, R.J., 2015. Slow magnetic Rossby waves in the earth's core, *Geophys. Res. Lett.,* **42**(16), 6622–6629.

King, E., Soderlund, K., Christensen, U., Wicht, J. & Aurnou, J., 2010. Convective heat transfer in planetary dynamo models, *Geochem. Geophys. Geosyst.,* **11** , doi:10.1029/2010GC003053.

Kloss, C., 2022. ancklo/chaosmagpy: Chaosmagpy v0.11, *Zenodo.*

Knezek, N. & Buffett, B., 2018. Influence of magnetic field configuration on magnetohydrodynamic waves in Earth's core, *Phys. Earth planet. Inter.,* **277**, 1–9.

Lecoanet, D., Le Bars, M., Burns, K.J., Vasil, G.M., Brown, B.P., Quataert, E. & Oishi, J.S., 2015. Numerical simulations of internal wave generation by convection in water, *Phys. Rev. E,* **91,** doi:10.1103/PhysRevE.91.063016.

Lighthill, M.J., 1952. On sound generated aerodynamically. I. General theory, *Proc. R. Soc. Lond., A,* **211**(1107), 564–587.

Livermore, P.W., Hollerbach, R. & Finlay, C.C., 2017. An accelerating high-latitude jet in Earth's core, *Nat. Geosci.,* **10**(1), 62–68.

Matsui, H., King, E. & Buffett, B., 2014. Multiscale convection in a geodynamo simulation with uniform heat flux along the outer boundary, *Geochem. Geophys. Geosyst.,* **15**(8), 3212–3225.

Maus, S., 2007. CHAMP, in *Encyclopedia of Geomagnetism and Paleomagnetism,* pp. 59–60, eds Gubbins, D. & Herrero-Bervera, E., Springer Netherlands.

Nicolas, Q., 2023a. qnicolas/macwaves: Second release, *Zenodo,* doi:10.5281/zenodo.7592767.

Nicolas, Q., 2023b. Dataset for "Excitation of high-latitude MAC waves in Earth's core", *Zenodo,* doi:10.5281/zenodo.7592727.

Olsen, N. *et al.*, 2000. Ørsted initial field model, *Geophys. Res. Lett.,* **27**(22), 3607–3610.

Schaeffer, N., Jault, D., Nataf, H.-C. & Fournier, A., 2017. Turbulent geodynamo simulations: a leap towards Earth's core, *J. geophys. Int.,* **211**(1), 1–29.

Schwaiger, T., Gastine, T. & Aubert, J., 2019. Force balance in numerical geodynamo simulations: a systematic study, *J. geophys. Int.,* **219**(Supplement 1), S101–S114.

van Tent, R., Deuss, A., Kaneshima, S. & Thomas, C., 2020. The signal of outermost-core stratification in body-wave and normal-mode data, *J. geophys. Int.,* **223**(2), 1338–1354.

Zhang, K., Earnshaw, P., Liao, X. & Busse, F.H., 2001. On inertial waves in a rotating fluid sphere, *J. Fluid Mech.,* **437**, 103–119.

APPENDIX: DERIVATION OF THE FORCED MAC WAVE EQUATION

The derivation follows Buffett & Matsui (2019), with additional terms coming from the forcings. The idea is to first use the hydrostatic constraint to eliminate pressure from the horizontal momentum equations, and subsequently substitute for the density perturbation using mass conservation. The background magnetic field B_{0r} is assumed uniform. After these two steps, the momentum equations become

$$\partial_t^2 \partial_r v_\theta - 2\Omega \cos\theta \, \partial_t \partial_r v_\lambda = \frac{N^2}{R} \partial_\theta v_r + \frac{B_{0r}}{\rho_0 \mu} \partial_t \partial_r^2 b_\theta$$
$$+ \partial_t \partial_r F_\theta - \frac{1}{R} \partial_t \partial_\theta F_r \qquad (A1)$$

and

$$\partial_t^2 \partial_r v_\lambda + 2\Omega \cos\theta \, \partial_t \partial_r v_\theta = \frac{N^2}{R \sin\theta} \partial_\lambda v_r + \frac{B_{0r}}{\rho_0 \mu} \partial_t \partial_r^2 b_\lambda$$
$$+ \partial_t \partial_r F_\lambda - \frac{1}{R \sin\theta} \partial_t \partial_\lambda F_r, \qquad (A2)$$

where the Brunt–Väisälä frequency is

$$N = \sqrt{-\frac{g}{\rho_0} \partial_r \rho_0}. \qquad (A3)$$

The solenoidal condition on $\boldsymbol{v}$ allows to express v_r as a function of the horizontal velocity components. To simplify its expression, we define $y = \cos\theta$ and note that $\partial_\theta = (1-y^2)^{\frac{1}{2}} \partial_y$; hence

$$\partial_r v_r = \frac{1}{R}(\partial_y v_\theta' - \partial_\lambda v_\lambda'), \qquad (A4)$$

where $v_\theta' = (1-y^2)^{\frac{1}{2}} v_\theta$, $v_\lambda' = (1-y^2)^{-\frac{1}{2}} v_\lambda$. We will similarly define b_θ', b_λ' as well as $F_{I\theta}'$ and $F_{I\lambda}'$. Substituting eq. (A4) into $(1-y^2)^{-\frac{1}{2}} \partial_r$ eq. (A1) and $(1-y^2)^{-\frac{1}{2}} \partial_r$ eq. (A2) yields

$$\partial_t^2 \partial_z^2 \left(v_\theta'(1-y^2)^{-1}\right) - 2\Omega y \partial_t \partial_z^2 v_\lambda'$$
$$= -\frac{N^2}{R^2} \partial_y \left(\partial_y v_\theta' - \partial_\lambda v_\lambda'\right) + \frac{B_{0r}}{\rho_0 \mu} \partial_t \partial_z^3 \left(b_\theta'(1-y^2)^{-1}\right)$$
$$+ (1-y^2)^{-\frac{1}{2}} \partial_t \partial_z^3 F_\theta + \frac{1}{R} \partial_t \partial_z \partial_y F_r \qquad (A5)$$

and

$$\partial_t^2 \partial_z^2 \left(v_\lambda'(1-y^2)\right) + 2\Omega y \partial_t \partial_z^2 v_\theta'$$
$$= \frac{N^2}{R^2} \partial_\lambda \left(\partial_y v_\theta' - \partial_\lambda v_\lambda'\right) + \frac{B_{0r}}{\rho_0 \mu} \partial_t \partial_z^3 \left(b_\lambda'(1-y^2)\right)$$
$$+ (1-y^2)^{\frac{1}{2}} \partial_t \partial_z^3 F_\lambda - \frac{1}{R} \partial_t \partial_z \partial_\lambda F_r, \qquad (A6)$$

where we have substituted ∂_z for ∂_r (recall that $z = r - R$). The next step involves eliminating the velocity variables using the induction equation. To simplify the expressions, we first Fourier-transform eqs (A5)–(A6) and (4). Transformed variables are denoted with tildes (see eq. 17); note that while $\boldsymbol{b}$, F_r and $\boldsymbol{F}_I$ are decomposed using half-range sine transforms, F_θ and F_λ are expressed with half-range cosine transforms, according to the parity of the number of radial differentiations applied to these terms. The induction eq. (4) now reads

$$-i\omega\chi \tilde{\boldsymbol{b}} = B_{0r} \widetilde{\partial_z \boldsymbol{v}} + \tilde{\boldsymbol{F}}_I \qquad (A7)$$

where χ is a damping term defined as

$$\chi = 1 + i\frac{\eta k^2}{\omega}. \qquad (A8)$$

Differentiating eqs (A5)−(A6) with respects to z, Fourier-transforming, plugging eq. (A7) and multiplying by $\frac{B_{0r} R^2}{i\omega\chi N^2}$ yields

$$-I(1-y^2)^{-1}\beta_\theta' + Ciy\beta_\lambda'$$
$$= d_y^2 \beta_\theta' - im d_y \beta_\lambda' - M(1-y^2)^{-1} \tilde{b}_\theta'$$
$$- A(1-y^2)^{-\frac{1}{2}} \tilde{F}_\theta + \frac{A}{Rk} d_y \tilde{F}_r, \qquad (A9)$$

$$-I(1-y^2)\beta_\lambda' - Ciy\beta_\theta'$$
$$= -im d_y \beta_\theta' - m^2 \beta_\lambda' - M(1-y^2)\tilde{b}_\lambda'$$
$$- A(1-y^2)^{\frac{1}{2}} \tilde{F}_\lambda - im \frac{A}{Rk} \tilde{F}_r, \qquad (A10)$$

where we have defined

$$\beta_\xi' = \tilde{b}_\xi' + \frac{\tilde{F}_{I\xi}'}{i\omega\chi} \quad \text{for } \xi = \theta, \lambda, \qquad (A11)$$

and the various parameters are

$$C = \frac{2\Omega\omega k^2 R^2}{N^2}, \ M = \frac{B_{0r}^2 k^4 R^2}{\rho_0 \mu \chi N^2}, \ I = \frac{R^2 \omega^2 k^2}{N^2}, \qquad (A12)$$

$$A = \frac{R^2 k^3 B_{0r}}{\chi N^2}. \qquad (A13)$$

With a radial field of 1 mT within a 140-km-thick layer, a wave of period 20 yr and radial wavenumber 1 has $|I/M| \simeq 0.01$, hence we can neglect the terms containing I. To see this, we rewrite eqs (A9)–(A10) as

$$\left(d_y^2 - (M-I)(1-y^2)^{-1}\right) \beta_\theta'$$
$$= i(Cy + m d_y)\beta_\lambda'$$
$$+ A(1-y^2)^{-\frac{1}{2}} \tilde{F}_\theta - \frac{A}{Rk} d_y \tilde{F}_r - M(1-y^2)^{-1} \frac{\tilde{F}_{I\theta}'}{i\omega\chi}, \qquad (A14)$$

$$\left(-m^2 - (M-I)(1-y^2)\right) \beta_\lambda'$$
$$= i(-Cy + m d_y)\beta_\theta'$$
$$+ A(1-y^2)^{\frac{1}{2}} \tilde{F}_\lambda + im \frac{A}{Rk} \tilde{F}_r - M(1-y^2)\frac{\tilde{F}_{I\lambda}'}{i\omega\chi}, \qquad (A15)$$

and substitute M for $M - I$. The next step consists in solving for $\tilde{\beta}_\lambda'$ in eq. (A15) and substituting in eq. (A14), then multiplying by $(m^2 + M(1-y^2))/M$. With $N \simeq \Omega$, M is of order 10^{-2}, hence terms in M/m^2 are neglected. We obtain:

$$(1-y^2)d_y^2 \beta_\theta' - 2y d_y \beta_\theta' + \left(\frac{C^2 y^2}{M} - \frac{m^2}{1-y^2} + \frac{mC}{M}\right) \beta_\theta'$$
$$= \frac{m^2}{M(1-y^2)^{\frac{1}{2}}} A\tilde{F}_\theta$$
$$- i\left(\left(\frac{C}{M} + \frac{2}{m}\right) y(1-y^2)^{\frac{1}{2}} + \frac{m}{M} d_y \left((1-y^2)^{\frac{1}{2}} \cdot\right)\right) A\tilde{F}_\lambda$$
$$+ \left(\left(\frac{mC}{M} + 2\right) y - (1-y^2)d_y\right) \frac{A}{Rk} \tilde{F}_r$$
$$- \frac{m^2}{1-y^2} \frac{\tilde{F}_{I\theta}'}{i\omega\chi}$$
$$+ i\left((1-y^2)(Cy + m d_y) - 2my\right) \frac{\tilde{F}_{I\lambda}'}{i\omega\chi} \qquad (A16)$$

For the final step, we define $\beta_\theta'' = (1-y^2)^{\frac{1}{2}} \beta_\theta'$, with similar definitions for $\tilde{b}_\theta''$ and $\tilde{F}_{I\theta}''$. This allows to get rid of the first order derivative in the right-hand side of eq. (A16) and yields a more compact expression. Substituting this definition, separating terms

in $\tilde{b}''_\theta$ and $\tilde{F}''_{I\theta}$, and dividing by $(1 - y^2)^{\frac{1}{2}}$ yields eq. (18), where the forcing term is given by

$$
\begin{aligned}
\mathcal{F} = {} & \frac{m^2}{M(1 - y^2)} A\tilde{F}_\theta \\
& - i \left(\left(\frac{C}{M} + \frac{2}{m} \right) y + \frac{m\,\mathrm{d}_y((1 - y^2)^{\frac{1}{2}} \cdot)}{M(1 - y^2)^{\frac{1}{2}}} \right) A\tilde{F}_\lambda \\
& + \left(\left(\frac{mC}{M} + 2 \right) \frac{y}{(1 - y^2)^{\frac{1}{2}}} - (1 - y^2)^{\frac{1}{2}}\,\mathrm{d}_y \right) \frac{A}{Rk} \tilde{F}_r \\
& - \frac{1}{i\omega\chi} \left(\mathrm{d}_y^2 + \frac{C^2 y^2 + mC}{M(1 - y^2)} + (1 - y^2)^{-2} \right) \tilde{F}''_{I\theta} \\
& + \frac{1}{\omega\chi} \left((1 - y^2)^{\frac{1}{2}} \left(m\,\mathrm{d}_y + Cy \right) - \frac{2my}{(1 - y^2)^{\frac{1}{2}}} \right) \tilde{F}'_{I\lambda}. \quad \text{(A17)}
\end{aligned}
$$